Nucleation of liquid bridges and bubbles in nanoscale capillaries

Aleksey Vishnyakov and Alexander V. Neimark[a)]
Center for Modeling and Characterization of Nanoporous Materials, TRI/Princeton, Princeton, New Jersey 08542

(Received 12 June 2003; accepted 13 August 2003)

Nucleation of liquid bridges and bubbles during condensation and evaporation of Lennard-Jones fluid in cylindrical pores is explored by Monte Carlo simulation. The isotherm of constrained critical nuclei is constructed using the gauge cell method. We confirm the Everett–Haynes scenario of bridging through the formation of a bump/undulation on the adsorption film. The molecular structure of growing bridges and cavitating bubbles is revealed. A new simulation approach is introduced to calculate the nucleation energy barriers. The method is based on the introduction and subsequent removal of a virtual ''ghost'' potential field with a tunable magnitude. Two computation schemes for determining the free energy of nuclei are elaborated based on the thermodynamic integration along a trajectory of states generated in the tunable ghost field and on the umbrella sampling. The methods developed are applicable to study various nucleation phenomena. © *2003 American Institute of Physics.* [DOI: 10.1063/1.1615760]

I. INTRODUCTION

Equilibrium, stability, and formation of liquid bridges between solid surfaces and in pores is one of the classical problems in colloid and interface science dating back to Plateau and Rayleigh.[1,2] Recently, this problem has attracted a lot of interest from both experimentalists and theoreticians. Experimental studies considered formation and snap-off of nanoscale liquid contacts between the sample and the tip in atomic force microscope and surface force apparatus, adhesion, nanotribology, nanolithorgaphy, and capillary condensation in pores of nanostructured materials.[3–10] Theoretical and simulation studies were concerned mostly with capillary condensation and cavitation in a gap between parallel solids surfaces. Landman[11] generated solidlike and liquidlike junctions by molecular dynamics (MD) simulations. Yasuoka *et al.*[12] studied formation and evolution of LJ clusters in a slit nanopore with wetting and nonwetting walls by MD simulations and estimated the nucleation rate from the cluster distribution. Capillary evaporation, accompanied with cavitation, in a lattice liquid confined to a slit pore was modeled by Luzar and Leung.[13,14] Bolhius and Chandler[15] investigated the dynamics of cavitation between liophobic surfaced by using the transition path sampling Monte Carlo (MC) technique. Stroud *et al.*[16] simulated formation and snap-off of bridges between nanoscale contacts by isostrain grand canonical MC technique. Other simulation studies considered two-stage capillary condensation and evaporation between chemically heterogeneous and corrugated surfaces. In this case formation of liquidlike bridges in the pore constrictions or in the regions with a stronger adsorption potential preceded condensation in the rest of the pore volume.[17–20] Also, nucleation in slit-shaped pores was studied by mean-field theories. Restagno *et al.*[21,22] attempted a numerical simulation of dynamics of capillary condensation in a gap with a time-dependent Ginzburg–Landau model. Talanquer and Oxtoby[22] exploited a two-dimensional local density functional theory (DFT) in the gradient approximation to examine possible pathways of nucleation between solvophobic walls and to estimate the free energy of nuclei.

Although capillary equilibrium in cylindrical nanopores was investigated in great details by various techniques (see, e.g., reviews of Gelb *et al.* and Neimark *et al.*[23,24] and references therein), studies of the pathways of phase transformations were limited to MC and MD simulations of spontaneous formation of periodic structures in quenched binary mixtures confined to long capillaries by Liu *et al.*,[25–27] Zhang and Chakrabarti,[28] and Gelb and Gubbins.[29,30] Recently, Vishnyakov and Neimark[31] simulated formation and evaporation of liquidlike bridges in short cylindrical necks of ink-bottle pores.

In the present work, we investigate the pathways of condensation and evaporation of a wetting fluid in a nanoscopic cylindrical pore, which are associated with formation and rapture of liquid bridges or vapor bubbles spanning the capillary cross section. Everett and Haynes[32] suggested the classical scenario of vapor condensation in a macroscopic cylindrical capillary (Fig. 1). They proposed that the liquid nucleation in a prewetted pore starts from a bumplike undulation, which grows and transforms into a lenslike bridge bounded by two hemispherical menisci. The bridge swells, menisci advance, and ultimately the pore is filled completely by condensed fluid. The transient unduloidal configurations have equicurvature interfaces with a constant capillary pressure which fulfills the Laplace equation, $P_{\mathrm{cap}} = -\gamma(r_1^{-1} + r_2^{-1}) = \text{constant}$, where γ is the liquid surface tension, and r_1 and r_2 are the main radii of curvature. The bump volume is a nonmonotonous function of the capillary pressure. The latter varies from the capillary pressure, $-\gamma/r$ (r is the pore radius), of the cylindrical interface of the wetting film for an infinitesimally small bump to the capillary pressure, $-2\gamma/r$,

a)Author to whom correspondence should be addressed. Electronic mail: aneimark@triprinceton.org

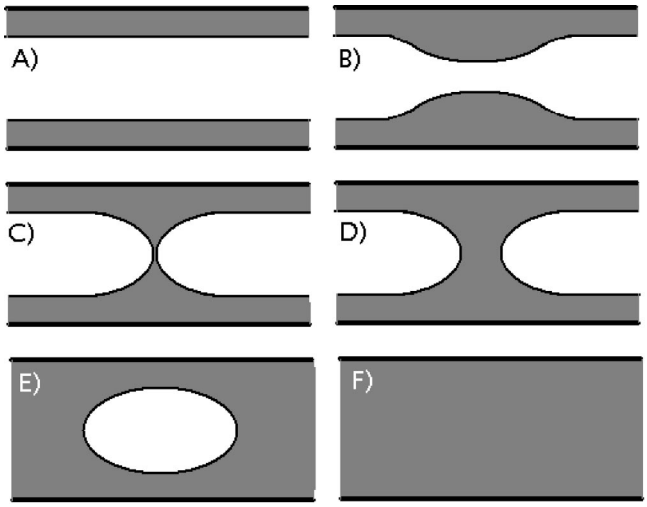

FIG. 1. The mechanism of capillary condensation in cylindrical pore with attractive walls according to the Everett–Haynes scenario (Ref. 34). (A) A laterally uniform adsorbed film (metastable vaporlike phase); (B) a liquidlike bump/undulation builds up breaking the symmetry; (C) the bump develops into a liquidlike bridge which spans the pore cross section; (D) the bridge grows; (E) the growth of bridges is accompanied by the contraction of bubbles; (F) the bubbles collapse and a laterally uniform liquidlike state is established. The reverse process of evaporation of condensed liquid starts from the cavitation of bubbles and ends by the snap-off of bridges and the relaxation of bumps.

of the hemispherical interface of the equilibrium meniscus for the limiting bump of the height approaching the pore radius. The most instructive conclusion of this scenario is that the critical nucleus of capillary condensation is the bump of maximum volume, rather than the lens of minimum volume that one would intuitively assume. Thus, capillary condensation in a cylindrical pore implies a morphological transition between laterally uniform configurations (adsorbed film coating the pore walls and condensed liquid filling the pore volume) through nonuniform configurations (bumps and bridges). This concept was recently elaborated by Kornev *et al.*,[33] who studied the bump-to-bridge evolution within the Derjaguin–Broechoff–deBoer (DBDB) theory,[34,35] which takes into account the stabilization of wetting films due to the action of the disjoining pressure. They showed that the spinodal of the DBDB equation of state, which determines the limit of stability of adsorbed films, is the bifurcation point that gives rise to symmetry breaking bumplike and periodic solutions.

We attempt to simulate the pathways of condensation and evaporation by the Monte Carlo (MC) technique. In doing so, we encounter a fundamental problem inherent to any nucleation phenomenon. Nuclei and transient states are unstable in an open system.[36,37] Thus, to study the pathways of phase transformations and to calculate the work of nucleation one has to trace thermodynamically metastable and unstable states. This can be done by imposing certain constraints on density fluctuations. In macroscopic thermodynamic models and mean-field approximations, such as the density functional theory, the constraints are enforced explicitly. In molecular simulations, the states of interest can be stabilized by restricting, in one way or another, the sampling in order to avoid their spontaneous destruction. Typically, the nuclei are modeled in the canonical NVT ensemble (e.g., Ref. 38) or generated in a homogeneous system using the umbrella sampling and configuration bias techniques.[39,40]

We employ the gauge cell MC simulation method,[41] which allows one to control the level of fluctuations and to generate at isothermal conditions a series of states with continuously varying average density. The models and simulation details are described in Sec. II. First, we construct the isotherm of laterally uniform states, which is an analog of the DBDB equation of state and has a form of a van der Waals loop. We determine the conditions of the vapor–liquid equilibrium, and the vaporlike and liquidlike spinodals (Sec. III). Second, we construct a trajectory of nonuniform states, which correspond to bumps, bridges, and bubbles, and show that the bump-to-bridge transformation follows qualitatively the Everett–Haynes scenario.[32] The free energy barriers for bridge condensation and bubble cavitation are determined by thermodynamic integration along this trajectory (Sec. IV). Third, we introduce a new technique named the ghost field method, which is based on thermodynamic integration and umbrella sampling methods. The ghost field method allows one to calculate the free energies of nucleation independently, in a regular manner (Sec. V). We conclude that the combination of the gauge cell and the ghost field methods provide a quantitative description of nucleation in nanoconfined fluids (Sec. VI).

It should be noted that the consideration of the capillary condensation in a cylindrical capillary as a phase transition between laterally uniform vaporlike and liquidlike states seems to be in an apparent contradiction with the rigorous statistical mechanical conclusion which forbids true phase transitions in one dimensional systems with short-range interactions.[42–44] To avoid possible confusions and misinterpretations let us recall that the Landau theorem[42] forbids thermodynamic equilibrium between two uniform semi-infinite phases, which are situated on a line and have a point contact, and an equilibrium state implies a domain system of certain concentration of interfaces between finite length vaporlike and liquidlike regions. In simulations with laterally periodic cells and in experiments with open-ended capillaries (even as long as those in MCM-41 materials with the ratio of the length-to-diameter ratio of the order of 10^3), one deals with essentially finite length systems which cannot be treated as quasi-one-dimensional. At subcritical conditions considered here, the equilibrium concentration of interfaces, which is reciprocal to the exponent of the interfacial free energy, is extremely low—many orders of magnitude smaller than the reciprocal length of the capillary under consideration. The objective of this work is to study the pathways of transitions between laterally uniform vaporlike and liquidlike states, which have practically ''infinite'' lifetime in the finite length systems at subcritical conditions. The near-critical behavior is beyond the scope of this paper.

II. MODEL SYSTEMS AND SIMULATION DETAILS

We consider capillary condensation of a Lennard-Jones (LJ) fluid in a cylindrical pore of ten molecular diameters in width, $2r=10\sigma$, with attractive LJ walls. The interaction parameters were chosen to mimic the experimentally rel-

evant system: Ar at its boiling temperature of 87.3 K within a nanopore typical for MCM-41 silica mesoporous molecular sieves. The LJ parameters for Ar were $\sigma=0.34$ nm and $\varepsilon/k=119.8$ K. The solid–fluid interactions were represented by the integrated LJ potential induced by the structureless cylindrical layer of oxygen atoms with solid–fluid parameters $\rho_s\varepsilon_{sf}/k=2253$ K/nm^2, $\sigma_{sf}=0.317$ nm (ρ_s is the surface density of attractive centers). As shown in Ref. 45, this model provides excellent agreement between the simulated equilibrium adsorption isotherm and the experimental isotherm MCM-41 sample with the average ''internal'' pore diameter of 3.17 nm.[46] Periodic boundary conditions were applied in the lateral direction z. We varied the lateral period l_z: Laterally uniform configurations were generated in ''short'' pores with of $l_z=10\sigma$, where the periodicity practically dictates the lateral uniformity of fluid configurations. For simulations of symmetry breaking configurations, longer simulation cells of $l_z=30\sigma$ were employed. As shown below, the lateral period does not affect any appreciably the generated adsorption isotherms of laterally uniform states.

In the gauge cell MC method,[41] the simulation is performed simultaneously in two cells, which are in chemical equilibrium at isothermal conditions. One of the cells represents the pore and the other is the gauge cell of a limited capacity. Mass exchange between the cells is allowed; however, the cell volumes are kept unchanged. The density fluctuations in the pore are controlled by the capacity of the gauge cell. In the limit of infinite capacity, the gauge cell method is equivalent to the grand canonical MC (GCMC) method. In the limit of vanishing capacity, it is equivalent to the canonical ensemble MC (CEMC) method. Choosing the ratio of the gauge cell and pore volumes sufficiently small, one can stabilize the fluid in the pore cell in a state, which would be unstable in the contact with the bulk. Thus, the gauge cell has two functions, to prevent nucleation and to measure the chemical potential of the pore fluid. The periodic boundary conditions provide additional constraints on the development of lateral wavelike fluctuations leading to spinodal decomposition.

A cube with triply periodic boundary conditions was employed as the gauge cell. The linear size of the gauge cell was at least 40 σ and was adjusted so that the sufficient number of fluid molecules was contained in the gauge cell during the simulation. The number of the molecules in the reference cell varied from 40 to 100. The standard simulation length was about 1×10^5 MC steps per molecule for laterally uniform configurations and 3×10^5 steps for bridge-type states. Each step included one attempt of a molecule displacement in each cell, and two attempts of molecule transfer between the cells (where applicable to the ensemble). The maximum number of molecules was about 1500 in simulations in the long pore of 30σ length.

III. LATERALLY UNIFORM CONFIGURATIONS: VAPOR–LIQUID EQUILIBRIUM AND SPINODALS

Using the GCMC (Ref. 47) and gauge cell MC methods we constructed a continuous, van der Waals-type isotherm of laterally uniform states in the short cell of lateral period $l_z=10\sigma$, which is smaller that the minimum wave length of

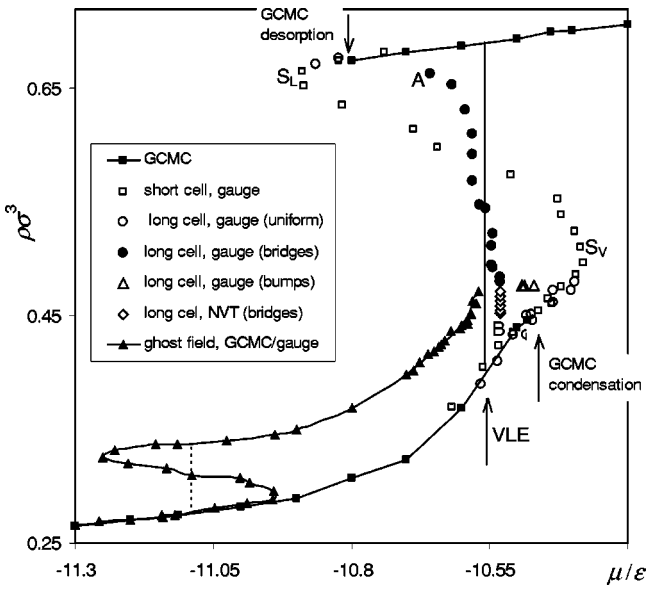

FIG. 2. Argon adsorption isotherms in 10σ cylindrical pore at $kT/\varepsilon=0.73$. Lines/closed squares: GCMC adsorption and desorption branches in a short cell (solid vertical line shows the vapor–liquid equilibrium in the pore); gray triangles: gauge cell method in a short cell; gray circles: laterally uniform configurations in a long cell obtained with the gauge cell method; open circles: bridgelike configurations in a long cell obtained with the gauge cell method; open triangles: bridgelike configurations in a long cell obtained using CEMC (these points drawn at the same chemical potential as the point of lowest density obtained with the gauge cell method, since m could not be estimated reliably in CEMC simulations); open squares: bumplike configurations obtained with the gauge cell method; solid lines/open diamonds: isotherm in a long cell with the ghost field obtained using GCMC and gauge cell method (dotted vertical line shows the formation/destruction of the bridge in GCMC simulation). Point A denotes the smallest bubble generated using gauge cell method; point B denotes the narrowest bridge generated in CEMC simulations; S_V and S_L denote vaporlike and liquidlike spinodals.

developing fluctuations. The laterally uniform states are shown in closed (GCMC) and open (gauge cell MC) squares in Fig. 2. In the CGMC simulation the fluid underwent spontaneous capillary condensation and evaporation transitions at $\mu=-10.48\varepsilon$ (from $\rho=0.446$ to $0.690\sigma^{-3}$), and $\mu=-10.82\varepsilon$ (from $\rho=0.674$ to $0.308\sigma^{-3}$), respectively. The laterally uniform states of intermediate density were constructed by the gauge cell method (open squares, Fig. 2). The results obtained with the two methods are in good agreement. The vaporlike spinodal S_V represents the limit of metastability of adsorption films. The liquidlike spinodal S_L represents the limit of metastability of stretched condensed fluid. The spinodals are connected by the backward trajectory of labile states of negative compressibility, which would be subject to the spinodal decomposition in a system unconstrained by periodic boundary conditions. In the following discussion, the ascending regions of the isotherm limited by the spinodals are called the adsorption and desorption branches. The former corresponds to stable and metastable films, or vaporlike states, the latter, to stable and metastable condensed fluid, or liquidlike states.

The chemical potential μ_e that corresponds to the vapor–liquid equilibrium (VLE) in the pore (more specifically, the condition of the equilibrium meniscus which would be determined in the Gibbs ensemble MC simulation as the

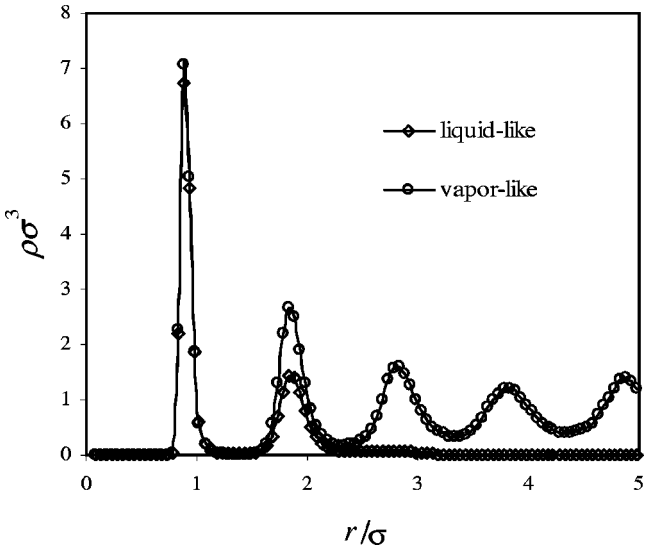

FIG. 3. Radial density profiles of laterally uniform vaporlike and liquidlike states in 10σ cylindrical pore at the vapor–liquid equilibrium. The liquidlike state consists of five distinct layers of molecules and the vaporlike state corresponds to the two layer adsorbed film.

equilibrium between the film and the condensed fluid in two pore cells), was obtained from the condition of equality of the grand thermodynamic potentials of equilibrium liquidlike and vaporlike states. The grand potential Ω was calculated by thermodynamic integration along the isotherm starting from a reference ideal gas state at a sufficiently low vapor pressure, $\Omega(\mu_r,T)=-kN_rT$,

$$\Omega(\mu,T)-\Omega(\mu_r,T)=-\int_{(\mu_r)}^{(\mu)}N(\mu,T)d\mu. \tag{1}$$

Then μ_e may be determined using the Maxwell rule of equal areas,

$$\oint_{\mu} Nd\mu=0. \tag{2}$$

The equilibrium chemical potential found, $\mu_e=-10.56\varepsilon$, shown in Fig. 2 by the black vertical line (for argon at 87.3 K this corresponds to $p_e=0.256$ atm), agrees with the result, $\mu_e=-10.53\varepsilon$, of the thermodynamic integration method of Peterson and Gubbins.[48] In order to implement the Peterson–Gubbins method, a supercritical isotherm at $kT/\varepsilon=1.38$ and a constant chemical potential path at $\mu=9.0\varepsilon$ were generated using the GCMC method. At the VLE, the fluid forms five distinct concentric layers in the liquidlike state and two layers in the vaporlike state demonstrated by density profiles shown in Fig. 3.

IV. BRIDGES, BUMPS, AND BUBBLES

The symmetry breaking is observed in the long pore of lateral period $l_z=30\sigma$. The adsorption and desorption branches of the isotherm (the results shown by gray circles in Fig. 2), practically coincide with the isotherm of laterally uniform states generated in the short pore, including the very vicinities of the spinodals. At the vaporlike spinodal, S_V, the fluid forms a uniform film on the pore wall that consists of two adsorbed layers, while the central part of the pore is filled with vapor. However, at the densities above ρ_{S_V}, the laterally uniform configuration is no more stable (even in the canonical ensemble). Starting from a uniform film, the fluid equilibrates to a nonuniform configuration in the form of a liquidlike bridge that spans the pore cross section. The density profile of a bridge is given in Fig. 4(A). Since the system is periodic in the lateral direction, this configuration is a periodical sequence of bridges and bubbles. The fluid in the center of the bridge is structured into five distinct layers; the radial density profile is close to that of the uniform liquidlike state at the same chemical potential. The menisci between the bridge and bubbles are visibly concave. Similar periodic configurations were observed in simulations of spinodal decomposition of binary solutions in cylindrical pores.[26,29]

The isotherm in the intermediate range of densities between the spinodals was constructed by adding and removing molecules via the gauge cell in small quantities. The isotherm has a sharp backward step in the vicinity of the VLE, which corresponds to the growing bridge in the process of condensation (density increases) or, vice versa, to the growing bubble in the process of evaporation (density decreases). Similarly to liquid droplets in supersaturated vapor and gas bubbles in stretched liquid, these states have negative compressibility; they are stable in the canonical ensemble and unstable in the grand canonical ensemble. In a sufficiently wide range of densities along the almost vertical part of the isotherm ($0.49\sigma^{-3}\leqslant\rho\leqslant0.61\sigma^{-3}$), the bridge width practically does not influence the shape of the meniscus and the densities in the middle of the bridge and in the center of the bubble. The substeps seen on the plot may lay within inherent computational error. This makes us believe that despite the finite length of the simulation cell and periodic boundary conditions, our simulations reveal the structure of the bridge–bubble interface correctly.

The stepwise trajectory of bridges is connected to the adsorption branch of uniform films through a series of states, depicted by open squares in Fig. 2, which can be thought as bumplike configurations. The density profile in Fig. 4(B) shows a bridgelike configuration, however the density in the pore center is significantly lower than the liquid density [compare to Fig. 4(A)]. If this configuration were treated in the framework of classical thermodynamics as a two phase system with the liquid–vapor interface drawn in accord with the Gibbs construction of dividing surfaces,[49] the liquid phase would be associated with a bump/undulation, and thus the continuity of the liquid phase in the pore cross section would be lost. This is an instructive example of limitations of the classical thermodynamics for description of nanoscale interfacial phenomena, even in a qualitative manner.

A. Nucleation barriers

Connecting the spinodals by a monotonously descending trajectory passing through the states of bubbles, bridges, and bumps, generated in the gauge cell MC simulation, we calculated the grand thermodynamic potential by integration according to Eq. (1). The results are given in Fig. 5 in comparison with the similar calculation for the laterally uniform

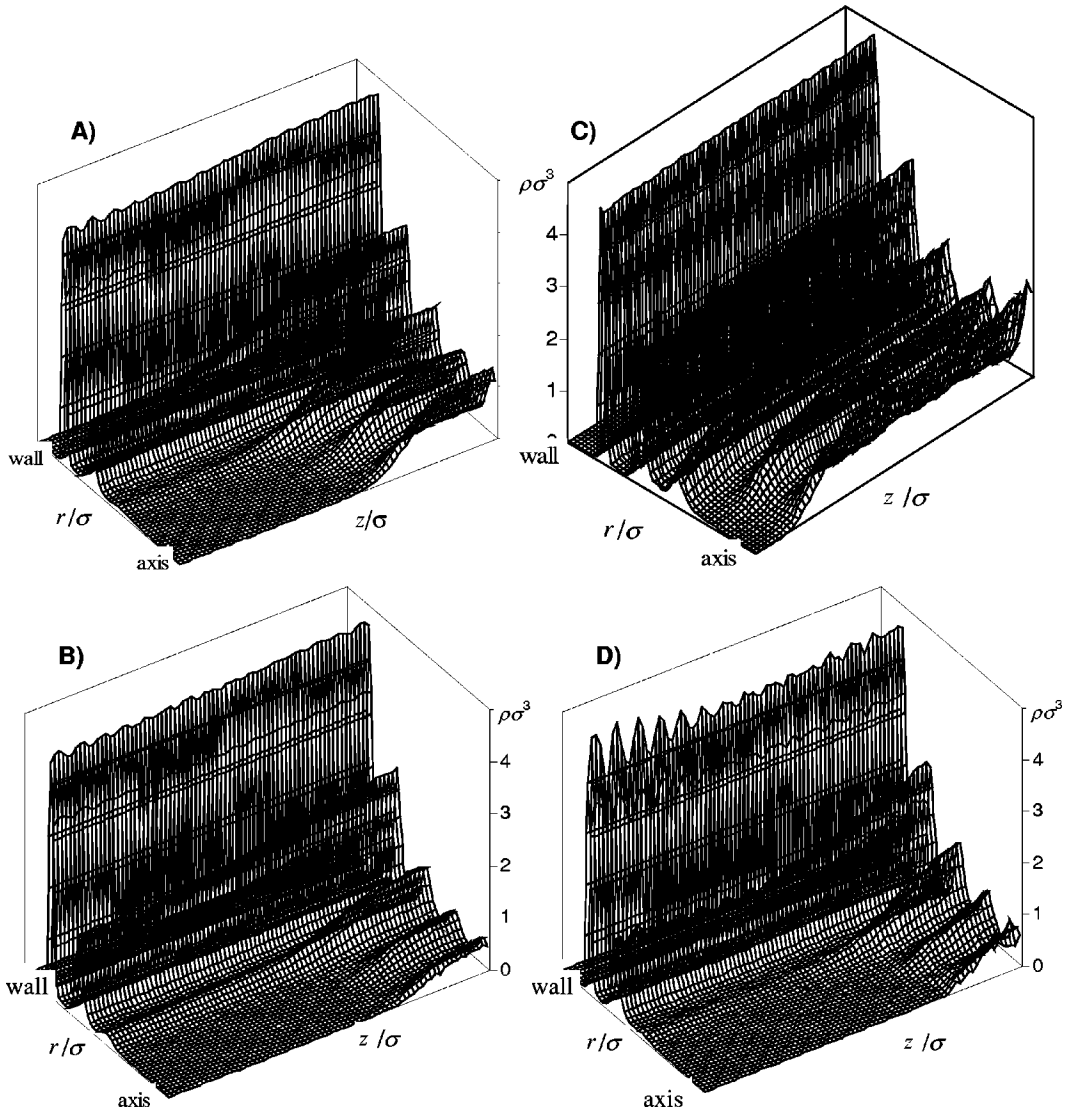

FIG. 4. Local density profiles of laterally nonuniform configurations. (A) Bridgelike configuration at $\mu=-10.55\varepsilon$, $\rho=0.488\sigma^{-3}$; (B) a bumplike configuration at $\mu=-10.48\varepsilon$, $\rho=0.475\sigma^{-3}$, where the density in the central part of the unduloid is substantially smaller than that in the liquidlike configuration at the same μ; (C) bubblelike configuration at $\mu=-10.66\varepsilon$, $\rho=0.662\sigma^{-3}$; (D) the narrowest bridge obtained in the canonical ensemble ($\rho=0.454\sigma^{-3}$).

states. The point of intersection of the grand thermodynamic potentials of uniform vaporlike and liquidlike states corresponds to the Maxwell rule and determines the VLE. As seen in the inset, the difference between the VLE points calculated from the two isotherms is very small (about 0.01ε or 0.5% in the vapor pressure of VLE, p_{VLE}), practically within the simulation error. This construction allows us to predict the free energy barriers of nucleation of bubbles and bridges, as the difference in grand thermodynamic potentials between nonuniform and uniform states at given external conditions, specified here by the chemical potential and temperature. Thus, the bridges/bumps and bubbles generated under constraints represent the critical nuclei of condensation and evaporation, respectively. The calculated nucleation barriers are given in Fig. 6. The right branch at $\mu_e<\mu<\mu_{sv}$ corresponds to the vapor-to-liquid nucleation via bridging, and the left branch at $\mu_{sv}<\mu<\mu_e$ corresponds to the liquid-to-vapor nucleation via cavitation,

$$\Delta\Omega_{vl}(\mu)=\Omega_{\mathrm{br}}(\mu)-\Omega_v(\mu), \tag{3a}$$

$$\Delta\Omega_{lv}(\mu)=\Omega_{\mathrm{bbl}}(\mu)-\Omega_l(\mu). \tag{3b}$$

The maximum, $\Delta\Omega_{vl}(\mu_e)=\Delta\Omega_{lv}(\mu_e)$, is achieved at the VLE, according to the Maxwell rule (2).

An analysis of the nucleation barriers gives an illuminative insight onto the hysteresis, which is commonly observed in virtual (GCMC simulations) and natural experiments. The maximum nucleation barrier in the system under consideration was approximately $20kT$, too high to be overcome in GCMC simulation within any reasonable CPU time. In our GCMC simulations of 12–50 million MC steps, the spontaneous condensation and evaporation transitions, indicated by vertical dotted lines in Fig. 6, occurred at the nucleation barriers of $3.6kT$ and $2.1kT$, respectively. At the same time the experimental isotherm of Ar at 87 K on a MCM-41 sample with the average pore internal diameter of 3.13 nm (the prototypical experimental system we attempted to simulate) is reversible.[50] This means, that at the typical conditions

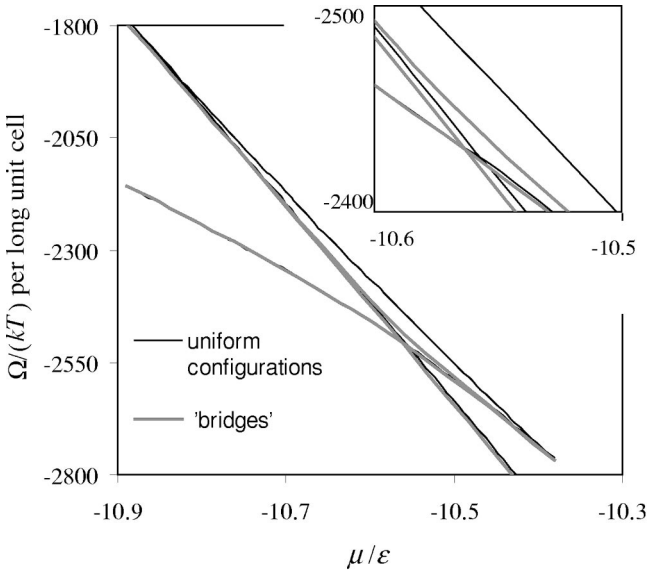

FIG. 5. Grand thermodynamic potentials obtained using the thermodynamic integration along the isotherms of laterally uniform and nonuniform configurations (bridges/bubbles/bumps). In the latter case the discontinuities of the isotherm were interpolated.

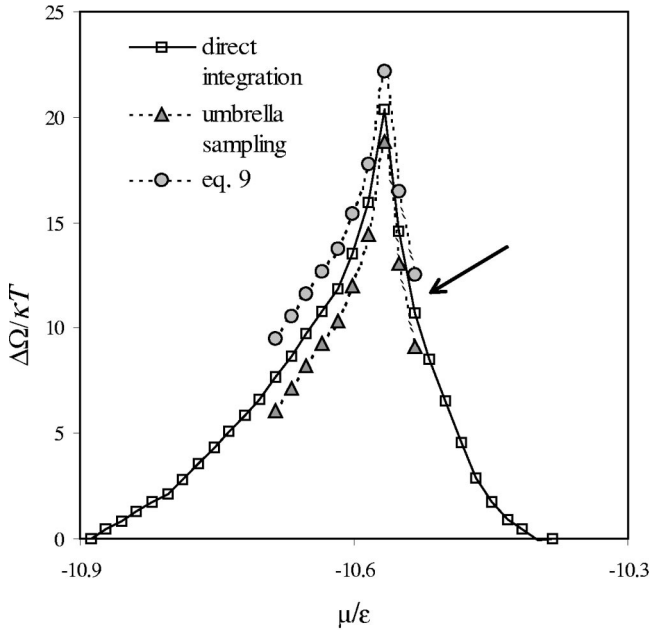

FIG. 6. The nucleation barriers for condensation (right branch) and evaporation (left branch) calculated using different methods. Squares: thermodynamic integration along the interpolated isotherm of bridges and bubbles generated by the gauge cell method [Eq. (4)]. Circles: thermodynamic integration along the ghost field isotherm [Eqs. (9)–(10)]. Triangles: umbrella sampling along the ghost field isotherm [Eqs. (13)–(14)]. The arrow marks the bridgelike configuration which was generated in the ghost field method. The maximum corresponds to the VLE.

and duration of adsorption experiments, the level of surmountable nucleation barriers far exceeds $20kT$.

B. Superspinodal behavior

In the gauge cell MC simulations, we could not avoid spontaneous transitions. Although, as shown below, these discontinuities did not affect the results of thermodynamic integration any appreciably, they are worth of thorough discussing.

Point A ($\rho=0.662\sigma^{-3}$) denotes the smallest bubble that was stabilized in the gauge cell simulation. Its density profile is shown in Fig. 4(C). The isotherm of bubbles could not be continued beyond this point to the vaporlike spinodal due to the superspinodal phenomenon described in detail in Ref. 51. Indeed, we were able to generate in CEMC simulation a bubblelike state of the density $\rho=0.667\sigma^{-3}$, which exceeds the spinodal density estimated as $\rho_{VS}=0.659\sigma^{-3}$. (This state is not shown in Fig. 2 since the chemical potential could not be determined in the canonical ensemble with required accuracy.) That is, in the density range $0.659\sigma^{-3}<\rho<0.667\sigma^{-3}$, there exists at least two states of equal density and different chemical potentials. Thus, the isotherm of bubbles is nonmonotonous. Its local maximum and minimum correspond to the superspinodals, the states of zero compressibility, which are not achievable. The region between the superspinodals does not contain the states corresponding to the local minima of the Helmholtz free energy, which could be stabilized in CEMC simulations.

The transition between the leftmost bumplike state ($\rho=0.476^{-3}$) with the smallest bridge stabilized in the gauge cell MC simulation ($\rho=0.479^{-3}$) resembles the bump-to-bridge transition of Everett and Haynes.[32] A series of CEMC simulations of bridgelike states of lower densities confirmed this hypothesis. Starting from $\rho=0.479\sigma^{-3}$, we gradually decreased the number of molecules in the pore by 5. The CEMC states are denoted by open triangles (the chemical potential in CEMC simulations could not be determined with required accuracy, and we placed these states underneath the smallest bridge with the gauge cell measured chemical potential). It is worth noting that for such a strongly inhomogeneous system, the Widom method for determining the chemical potential[52] gives an error far exceeding the deviations inherent to the gauge cell method. The limit of stability of bridges in the canonical ensemble (point B) was estimated as $\rho=0.452\sigma^{-3}$, which is considerably lower than the density of the bumplike configurations (Fig. 2). The density profile shown in Fig. 4(D) does not allow us to assign to this bridge any width, and the density in the middle of the bridge is lower than the liquid density that shows a gradual approach to bump-type configurations.

Thus, the isotherm of nonuniform configurations in the region of the bump-to-bridge transition is nonmonotonous and is qualitatively similar to that described by Everett and Haynes.[32] The minimum corresponding to the smallest bridge and the maximum corresponding to the largest bump limit the states stabilizable in the canonical ensemble. Thus, the state of the largest bump has zero compressibility and represents a superspinodal. The bump cannot be grown up beyond the superspinodal, it will be inevitably transformed into a bridge of the same average density with a gain in the free energy.

As the density decreases, the bump undergoes a spontaneous transition from the bumplike configuration to the uniform film. Since we were unable to generate any additional bumplike states, we can only hypothesize that this transition

indicates the existence of another superspinodal state of zero compressibility, which limits the density of stabilizable bumplike configurations from below.

Note that the multiplicity of states of equal density and corresponding superspinodal behavior[51] are characteristic of phase transitions in finite volumes. Recently, Riguera *et al.*[53] considered droplet nucleation in a finite reservoir of a supersaturated vapor. Keeping fixed the total number of molecules, they constructed a $p-V$ isotherm with two solutions that corresponded to ''small'' and ''big'' droplets. Therefore, small droplets, that are unstable in the canonical ensemble are separated from metastable big droplets by a state of zero compressibility, which in accepted terminology here are called superspinodals.[51] The configurations located between the superspinodals correspond to local maxima of the Helmholtz free energy and therefore cannot be stabilized by constraints on density imposed in the canonical ensemble or the gauge cell MC simulations.[51]

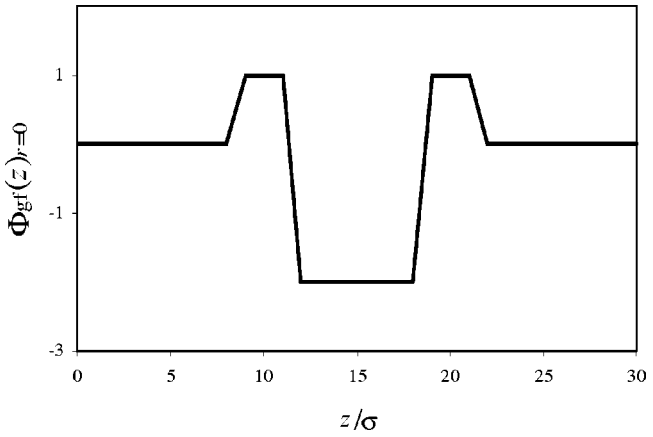

FIG. 7. Profile of the ghost field along the pore axis ($r=0$): a potential well, where the liquidlike bridge is formed, is surrounded by potential barriers to prevent the bridge growth beyond a desired size. The total external potential in the pore is a sum of the solid–fluid potential and the ghost field.

V. THE GHOST FIELD METHOD

In order to calculate the nucleation barriers in a rigorous fashion, using thermodynamic integration without an interpolation of the isotherm through the regions of spontaneous transitions, one has to construct a continuous trajectory of equilibrium states, which connects a bridgelike configuration to a reference state the free energy of which is known. For this purpose, we elaborated on a special technique using the ideas of thermodynamic integration and umbrella sampling method.[54,55] In this technique, we introduce a virtual external attractive field with a potential well localized in the pore center, which is named the ghost field. The magnitude of the ghost field is tunable. Once switched on, the ghost field facilitates the vapor condensation in the potential well. In the presence of the ghost field, a bridge of a given size is formed continuously in a series of GCMC or gauge cell simulations, as the vapor pressure increases. Once the desired configuration is achieved, the ghost field is turned off gradually, step by step in a series of CEMC simulations. The difference of the free energies of the bridge with and without the ghost field is calculated using the methods described below.

In the ghost field method, the fluid is subjected to the total external potential field which is a sum of the adsorption potential from the pore walls $\Phi_{SF}(\mathbf{r})$ (see Sec. II) and the tunable ghost field $\Phi_G(\mathbf{r}):\Phi_{\text{ext}}(\mathbf{r})=\Phi_{SF}(\mathbf{r})+\zeta\Phi_G(\mathbf{r})$, where ζ is the ghost field magnitude, $0<\zeta<1$. $\zeta=1$ corresponds to the full scale ghost field, $\zeta=0$ corresponds to its absence. The ghost field $\Phi_G(\mathbf{r})$ was chosen for the sake of convenience as follows (Fig. 7). In the center of the basic cell, we created a potential well of -2ε depth and 3σ width (in the lateral direction). Small potential barriers of ε height and 2σ width were created on both sides of the well in order to prevent the bridge growth. The continuity of the total potential in the radial direction was secured using transition zones between different areas (Fig. 7).

The adsorption isotherm $N_G(\mu)$ in the cell with the ghost field ($\zeta=1$) obtained using GCMC and the gauge cell method is shown in Fig. 2 by open triangles. The equilibrium transition from a laterally uniform film to a bridge-type configuration takes place at $\mu\approx-11.1\varepsilon$. The bridge is formed in the potential well, while the barriers prevent its expansion. At $\mu=\mu_{\zeta=1}=-10.58\varepsilon$, the configuration of the bridge generated with the ghost field resembles the corresponding bridgelike configuration of the same density $\rho=0.488\sigma^{-3}$ obtained without the ghost field at $\mu=\mu_{\zeta=0}=-10.53\varepsilon$. However, the bridge formed in the ghost field has higher density in the center due to the potential well and distinct boundaries caused by the repulsive bands that prevent bridge growth (Fig. 8). The free energy of the fluid in the ghost field can be calculated by the thermodynamic integration along the constructed continuous isotherm via Eq. (1),

$$F(N,V,T,1)=F_G(N,V,T)=\Omega_G(\mu_r,T)-\int_{(\mu_r)}^{(\mu)}N_G(\mu,T)d\mu+\mu N. \tag{4}$$

In the subsequent series of CEMC simulations the ghost field has been gradually removed by incremental decreasing the tuning parameter ζ from 1 to 0. The Helmholtz free energy, $F(N,V,T,\zeta)$, of the fluid in the ghost field of the magnitude ζ, is defined through the canonical partition function:

$$Q(N,V,T,\zeta)=\frac{1}{\Lambda^{3N}N!}\int d\mathbf{r}^N\times\exp(-(\Phi(\mathbf{r}^N)+\zeta\Phi_G(\mathbf{r}^N))/kT), \tag{5}$$

where $\Phi(\mathbf{r}^N)=\Phi_{FF}(\mathbf{r}^N)+\Phi_{SF}(\mathbf{r}^N)$, as

$$F(N,V,T,\zeta)=-kT\ln Q(N,V,T,\zeta). \tag{6}$$

The derivative of $F(N,V,T,\zeta)$ with respect to the host field magnitude is represented as the ensemble average of the host field,

$$\left.\frac{\partial F}{\partial\zeta}\right|_{N,V,T}=-kT\frac{1}{Q}\left.\frac{\partial Q}{\partial\zeta}\right|_{N,V,T}=\frac{\int d\mathbf{r}^N\Phi_G(\mathbf{r}^N)\exp(-(\Phi(\mathbf{r}^N)+\zeta\Phi_G(\mathbf{r}^N))/kT)}{\int d\mathbf{r}^N\exp(-(\Phi(\mathbf{r}^N)+\zeta\Phi_G(\mathbf{r}^N))/kT)}=\langle\Phi_G\rangle_{N,V,T,\zeta}. \tag{7}$$

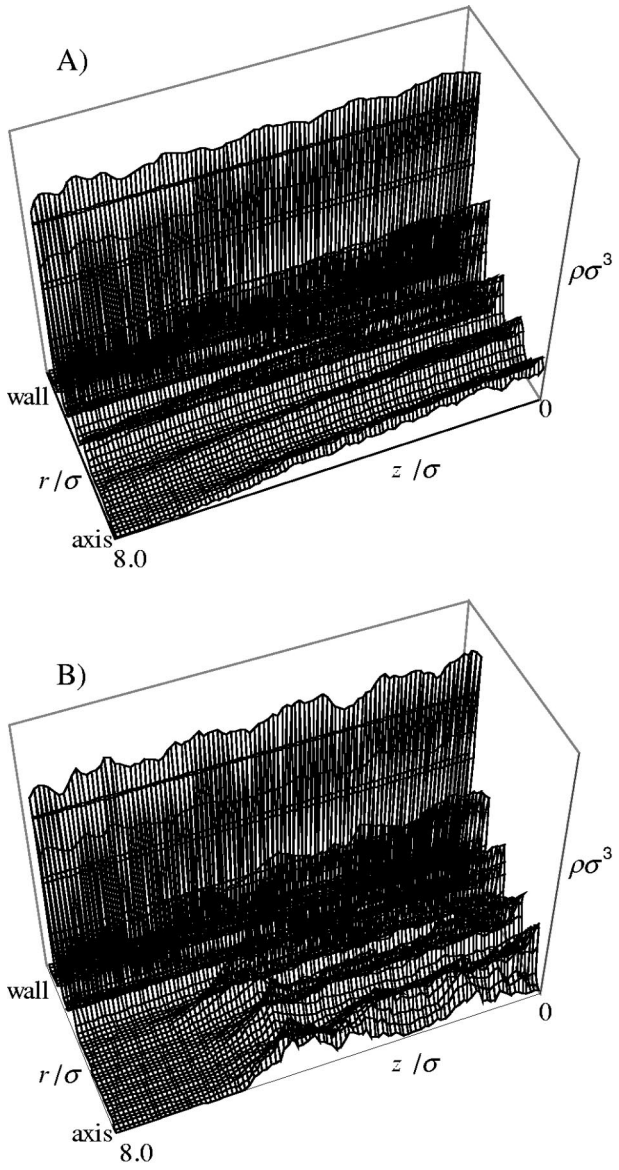

FIG. 8. Local density profiles of the bridgelike configurations at $\rho = 0.488\sigma^{-3}$. (A) Without the ghost field ($\zeta=0$) and (B) with the ghost field ($\zeta=1$).

Here $\langle\Phi_G\rangle_{N,V,T,\zeta}$ denotes the canonical ensemble average for the fluid in the ghost field of the magnitude ζ. It can be calculated by weighting the host field with the average fluid density $\rho\zeta(\mathbf{r})$ in the ghost field of the magnitude ζ,

$$\langle\Phi_G\rangle_{N,V,T,\zeta} = \int_V \Phi_G(\mathbf{r})\rho_\zeta(\mathbf{r})d^3r. \tag{8}$$

Integration of Eq. (6) along the CEMC trajectory gives a practical formula for calculating the Helmholtz free energy, $F(N,V,T,\zeta)$,

$$F(N,V,T,\zeta) = F(N,V,T,1) - \int_\zeta^1 \langle\Phi_G\rangle_{N,V,T,\zeta} d\zeta$$

$$= F_G(N,V,T) = -\int_V \Phi_G(\mathbf{r})\rho_\zeta(\mathbf{r})d^3r. \tag{9}$$

Thus, the sought Helmholtz free energy of the bridge without the ghost field $F(N,V,T) = F(N,V,T,0)$, is given by

$$F(N,V,T) = F_G(N,V,T) - \int_0^1 \langle\Phi_G\rangle_\zeta d\zeta. \tag{10}$$

Equation (10) implies numerical integration which accuracy depends on the number of CEMC simulations at different $\zeta = 1,...,\zeta_I,\zeta_{I+1},\ldots,0$.

To check the thermodynamic integration accuracy we employ the umbrella sampling technique of Torrie and Valleau[54] to calculate the Helmholtz free energy (see Ref. 55). Starting from Eqs. (4) and (5), the incremental difference in the Helmholtz free energy of two states with the ghost field magnitudes ζ_i and ζ_{i+1}, $\Delta F_{i+1,i}$, equals

$$\Delta F_{i+1,i} = -kT \ln \frac{\int d\mathbf{r}^N \exp(-(\Phi(\mathbf{r}^N) + \zeta_{i+1}\Phi_G(\mathbf{r}^N))/kT)}{\int d\mathbf{r}^N \exp(-(\Phi(\mathbf{r}^N) + \zeta_i\Phi_G(\mathbf{r}^N))/kT)}. \tag{11}$$

$\Delta F_{i+1,i}$ can be expressed through the ensemble average performed in CEMC simulation at $\zeta=\zeta_i$ as

$$\Delta F_{i+1,i} = -kT \ln\langle\exp(-(\zeta_{i+1}-\zeta_i)\Phi_G/kT)\rangle_{\zeta_i}. \tag{12}$$

However, the best estimate is achieved by using ensemble average performed in CEMC simulation with the ghost field of the intermediate magnitude $\zeta_i^* = \zeta_I + (\zeta_{i+1} - \zeta_I)/2$ in the form

$$\Delta F_i = -kT \ln \frac{\langle\exp(-(\zeta_{i+1}-\zeta_i^*)\Phi_G/kT)\rangle_{\zeta_i^*}}{\langle\exp((\zeta_i^*-\zeta_i)\Phi_G/kT)\rangle_{\zeta_i^*}}. \tag{13}$$

This choice provides a better overlapping of sampled configurations. The total change of the Helmholtz free energy of the fluid is given by

$$F(N,V,T) = F_G(N,V,T) - \sum_i \Delta F_i. \tag{14}$$

In the limit of $\beta(\zeta_{i+1}-\zeta_i)\Phi_G \ll 1$, both methods, Eq. (10) and Eqs. (13)–(14), are precise and give identical results. This is seen from the expansion of the exponent and then the logarithm in Eqs. (12)–(14) into the Tailor set, namely,

$$-kT\sum_i \ln\langle\exp(-(\zeta_{i+1}-\zeta_i)\Phi_G/kT)\rangle_{\zeta_i}$$

$$\approx -\sum_i (\zeta_{i+1}-\zeta_i)\langle\Phi_G\rangle_{\zeta_i} \approx -\int_\zeta^1 \langle\Phi_G\rangle_\zeta d\zeta. \tag{15}$$

In practice the ghost field method was implemented as follows. The difference of free energies of the bridgelike configurations with and without the ghost field was estimated at $\rho = 0.488\sigma^{-3}$ using a series of ten CEMC simulations by reducing ζ from 0.95 to 0.05. Therefore, the chemical potential is increased from $\mu_{\zeta=1} = -10.56\varepsilon$ to $\mu_{\zeta=0} = -10.53\varepsilon$, while $N_G(\mu_{\zeta=1}) = N_G(\mu_{\zeta=1}) = N_{\mathrm{br}}$. The CEMC steps were generated using regular canonical ensemble sampling with the canonical weighting function at ζ_I^*. At each step, the

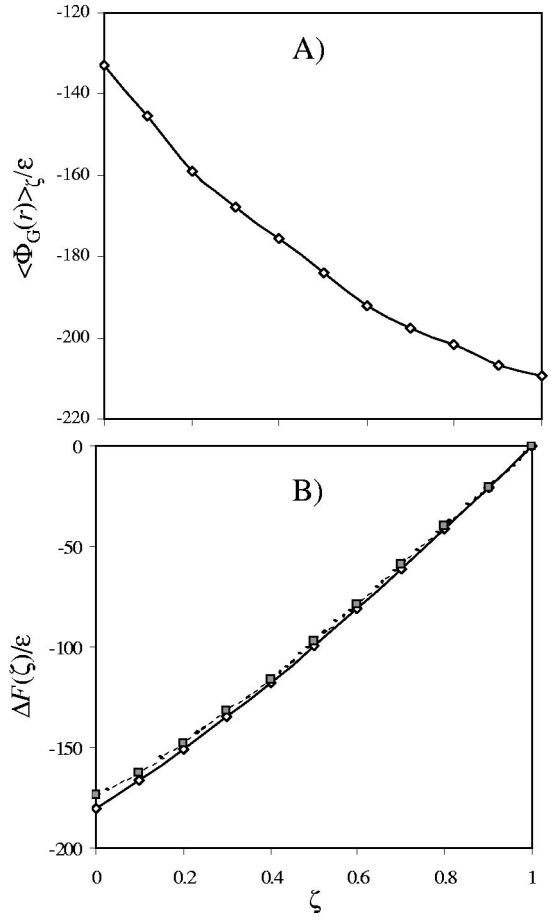

FIG. 9. Calculations of the Helmholtz free energy of the ghost field "removal" $\Delta F = F(N,V,T) - F_G(N,V,T)$ at $\rho\sigma^3 = 0.488$. (A) $\langle \Phi_G \rangle_\zeta$, the energy of the fluid interaction with the ghost field averaged over configurations obtained at $0 \leqslant \zeta \leqslant 1$. $\zeta = 0$ corresponds to the "undisturbed" bridge with no ghost field with the ghost field, $\zeta = 1$ corresponds to the bridge generated in the ghost field. (B) $\Delta F = F(N,V,T,1) - F(N,V,T,\zeta)$ obtained using direct integration (squares) and umbrella sampling (diamonds).

free energy difference ΔF_i between the states $\zeta_i^* - 0.05$ and $\zeta_i^* + 0.05$ For example, $\zeta^* + 0.45$, internal energies for $\zeta = 0.4$ and $\zeta = 0.5$ was calculated according to Eq. (13). The difference in the grand potential between the bridge-type configuration in the cell with ghost field ($\zeta = 1$) and without it ($\zeta = 0$) was estimated as

$$\Delta\Omega_{1-0} = \int_1^0 \left(\frac{\partial F}{\partial \zeta} \right)_{\mathrm{NVT}} d\zeta - N(\mu_{\zeta=1} - \mu_{\zeta=0}) \approx \sum_{j=1}^{10} \Delta F_j - N(\mu_{\zeta=1} - \mu_{\zeta=0}). \quad (16)$$

Figure 9 demonstrates the evaluation of $F(N,V,T) - F_G(N,V,T)$ with both methods: the integration of $\langle \Phi_G \rangle_\zeta$ over ζ and umbrella sampling. $\langle \Phi_G \rangle_\zeta$ is shown in Fig. 9(A). $\langle \Phi_G \rangle_\zeta$, decreases monotonously from $\zeta = 1$ to $\zeta = 0$. Since $\langle \Phi_G \rangle_\zeta$ at $\zeta = 0$ is the energy of the fluid interaction with the ghost field of the magnitude 1 averaged over configurations obtained at $\zeta = 0$ (that is, over the bridge undisturbed with the ghost field), because of a redistribution of molecules within the bridge.

Figure 9(B) shows the result of integration over ζ [Eq. (10)] and the umbrella sampling method [Eqs. (13)–(14)]. The two methods agree reasonably with each other, giving $F(N,V,T) - F_G(N,V,T) = -180.1$ and -177.9ε, respectively. The umbrella sampling technique predicts larger free energy difference that seems to be a result of a systematic statistical error, which is likely caused by an imperfect overlap of configurations sampled at different ζ. The potential barrier associated with the formation of a bridge at $\mu = -10.53\varepsilon$ is calculated according to Eqs. (4) and (16). For $\rho\sigma^3 = 0.488$, we obtain the grand potential of the bridgelike configuration at $\zeta = 1$ of -1959.1ε using Eq. (4), $(\mu_{\zeta=0} - \mu_{\zeta=1}) N_{\mathrm{br}} = 38.0\varepsilon$, $\Omega(\mu_{\zeta=0}) = -1826.1\varepsilon$, that is, for the formation of the bridge $\Delta\Omega = 9.1\varepsilon = 12.5kT$ using Eq. (10) and $6.9\varepsilon = 9.2kT$ using Eq. (13).

Using the bridge state at $\mu_{\zeta=0} = -10.53\varepsilon$ as a reference state, the grand potential $\Omega(\mu,T)$ of bridges and bubbles along the continuous portion of the gauge cell isotherm was calculated via Eq. (1). Then the nucleation barriers $\Delta\Omega(\mu)$ were calculated using Eq. (3). The dependencies $\Delta\Omega(\mu)$ determined by the thermodynamic integration and umbrella sampling techniques are shown in Fig. 6. Accounting for inherent errors of computations, the agreement with the results of thermodynamic integration along the extrapolated gauge cell isotherm is quite satisfactory. We may conclude that in the case under consideration, the method developed for calculating the nucleation barriers provided a reasonable accuracy of $\approx 10\%$.

VI. CONCLUSIONS

The processes of nucleation of liquid bridges and bubbles in a nanoscale cylindrical pore were studied by using a combination of grand canonical, canonical ensemble, and gauge cell MC simulation methods. Considering, as a case study, capillary condensation and evaporation of a LJ model of Ar in a silica channel of ten Ar molecular diameters in width, we investigated the pathways of vapor–liquid and liquid–vapor transitions and determined the nucleation mechanisms and the nucleation barriers. We confirmed the Everett–Haynes scenario of capillary condensation as a symmetry breaking morphological transition between laterally uniform configurations of adsorbed films and condensed liquid through nonuniform bridgelike configurations. Therefore, the development of a bumplike undulation of the adsorbed film precedes the bridge formation. The growth of bridges is accompanied by the contraction of bubbles between them. The reverse process of evaporation starts from the cavitation of bubbles and ends up with the snap-off of interbubble bridges. Simulations revealed the molecular structure of growing bridges and cavitating bubbles.

Since nuclei and transient states are intrinsically unstable in an open system, certain constraints must be imposed in order to generate and stabilize them in molecular simulations. The problem of stabilization of thermodynamically labile states was solved by the gauge cell MC simulation technique developed recently.[41] With the gauge cell method, we control the level of admissible fluctuations in the system and avoid spontaneous transitions inherent to GCMC. By varying the length of the simulation cell, we constructed two van der

Waals-type sigmoid isotherms: (i) of laterally uniform states in the short cell and (ii) of nonuniform configurations of bumps, bridges, and bubbles in the long cell. The vaporlike and liquidlike spinodals were determined from the turnover points of the isotherm of the laterally uniform states. The vaporlike spinodal corresponds to the limit of stability of metastable adsorption films; the liquidlike spinodal corresponds to the limit of stability of stretched condensed liquid. The VLE was determined from the Maxwell rule by the thermodynamic integration along the isotherm of labile states which continuously connected the spinodals.

The isotherm of nonuniform states was shown to be a multivalued function in the regions near the spinodals. This behavior between the vaporlike spinodal and VLE is consistent with the Everett–Haynes bump-to-bridge transition. The bump of maximum density and the bridge of minimum density corresponds to the states of zero compressibility which cannot be achieved in CEMC simulations. These superspinodal states correspond to the limits of stabilization of labile configurations in the canonical ensemble. States of intermediate density between the superspinodals cannot be generated. Similar superspinodal behavior was observed in the region of bubble cavitation, near the liquidlike spinodal. Interpolating the isotherm in the superspinodal regions, we calculated the grand thermodynamic potential for bridges and bubbles and determined the VLE, which agreed with the VLE calculated from the isotherm of uniform states. Then, the nucleation barriers were calculated from the difference of the grand potentials between the state with the nucleus and the metastable uniform state at the given chemical potential.

A ghost field method was developed to calculate the nucleation barriers avoiding interpolation of the bridge-bump isotherm. First, one generates the nucleus of a given density in a continuous manner by introducing a virtual external attractive field of a tunable magnitude. This is done in a series of GCMC or gauge cell simulations. Second, the ghost field is gradually removed in a series of CEMC simulations, and the nucleus without the ghost field is stabilized in the gauge cell simulation. Two computation schemes were elaborated for determining the free energy of the nucleus formation. One is based on direct thermodynamic integration along the isotherm in the tunable ghost field. The other exploits the umbrella sampling method for calculating the free energy difference. The nucleation barriers for condensation of bridges and cavitation of bubbles determined by the methods developed are within reasonable error bars.

We conclude that the combination of the gauge cell and the ghost field methods provide a quantitative description of nucleation in nanoconfined fluids and hysteretic phase transitions observed in finite size systems. The methods developed can be recommended to molecular simulation studies of various nucleation phenomena, including nucleation of droplets and bubbles in different confinements and environments.

[1] J. A. Plateau, *Statique Expérimentale et Théorique des Liquides Soumis aux Seules Forces Moléculaires* (Gautier-Villars, Paris, 1873).
[2] J. W. S. Rayleigh, Proc. R. Soc. London **29**, 71 (1879).
[3] M. Heuberge, M. Zach, and N. D. Spencer, Science **292**, 905 (2001).
[4] M. Y. He, A. S. Blum, D. E. Aston *et al.*, J. Chem. Phys. **114**, 1355 (2001).
[5] N. Maeda and J. N. Israelachvili, J. Phys. Chem. B **106**, 3534 (2002).
[6] C. D. Willet, M. J. Adams, S. A. Johnson *et al.*, Langmuir **16**, 9396 (2000).
[7] N. M. Patel, M. R. Dodge, J. I. D. Alexander *et al.*, Phys. Rev. E **65**, 026306 (2002).
[8] M. Y. Lin, S. K. Sinha, J. M. Drake *et al.*, Phys. Rev. Lett. **72**, 2207 (1994).
[9] Y. Gogotsi, J. Libera, A. Güvenç-Yazicioglu *et al.*, Appl. Phys. Lett. **79**, 1021 (2001).
[10] J. Jang, G. C. Schatz, and M. A. Ratner, Phys. Rev. Lett. **90**, 156401 (2003).
[11] U. Landman, Solid State Commun. **107**, 693 (1998).
[12] K. Yasuoka, G. T. Gao, and X. C. Zeng, J. Chem. Phys. **112**, 4279 (2000).
[13] A. Luzar and K. Leung, J. Chem. Phys. **113**, 5836 (2000).
[14] K. Leung and A. Luzar, J. Chem. Phys. **113**, 5845 (2000).
[15] P. G. Bolhuis and D. Chandler, J. Chem. Phys. **113**, 8154 (2000).
[16] W. J. Stroud, J. E. Curry, and J. H. Cushman, Langmuir **17**, 688 (2001).
[17] W. Gac, A. Patrykiejew, and S. Sokolowski, Surf. Sci. **306**, 434 (1994).
[18] A. Vishnyakov, E. M. Piotrovskaya, and E. N. Brodskaya, Adsorption **4**, 207 (1998).
[19] H. Bock and M. Schoen, Phys. Rev. E **59**, 4122 (1999).
[20] M. Schoen, Colloids Surf., A **206**, 253 (2002).
[21] F. Restagno, L. Bocquet, and T. Biben, Phys. Rev. Lett. **84**, 2433 (2000).
[22] V. Talanquer and D. W. Oxtoby, J. Chem. Phys. **114**, 2793 (2001).
[23] L. D. Gelb, K. E. Gubbins, R. Radhakrishnan *et al.*, Rep. Prog. Phys. **62**, 1573 (1999).
[24] A. V. Neimark, P. I. Ravikovitch, and A. Vishnyakov, J. Phys.: Condens. Matter **15**, 347 (2003).
[25] A. J. Liu, D. J. Durian, E. Herbolzheimer *et al.*, Phys. Rev. Lett. **65**, 1897 (1990).
[26] A. J. Liu and G. S. Grest, Phys. Rev. A **44**, R7894 (1991).
[27] L. Monette, A. J. Liu, and G. S. Grest, Phys. Rev. A **46**, 7664 (1992).
[28] Z. Zhang and A. Chakrabarti, Phys. Rev. E **50**, R4290 (1994).
[29] L. D. Gelb and K. E. Gubbins, Phys. Rev. E **56**, 3185 (1997).
[30] L. D. Gelb and K. E. Gubbins, Physica A **244**, 112 (1997).
[31] A. Vishnyakov and A. V. Neimark, Langmuir **19**, 3240 (2003).
[32] D. H. Everett and J. M. Haynes, J. Colloid Interface Sci. **38**, 125 (1972).
[33] K. G. Kornev, I. K. Shingareva, and A. V. Neimark, Adv. Colloid Interface Sci. **96**, 143 (2002).
[34] B. V. Derjaguin, Acta Physicochim. URSS **12**, 181 (1940).
[35] J. C. P. Broekhof and J. H. deBoer, J. Catal. **9**, 8 (1967).
[36] J. S. Rowlinson and B. Widom, *Molecular Theory of Capillarity* (Clarendon, Oxford, 1982).
[37] H. Reiss, *Methods of Thermodynamics* (Blaisdell, New York, 1965).
[38] A. I. Rusanov and E. N. Brodskaya, J. Colloid Interface Sci. **62**, 542 (1977).
[39] V. K. Shen and P. G. Debenedetti, J. Chem. Phys. **111**, 3581 (1999).
[40] P. R. tenWolde and D. Frenkel, J. Chem. Phys. **109**, 9901 (1998).
[41] A. V. Neimark and A. Vishnyakov, Phys. Rev. E **62**, 4611 (2000).
[42] L. D. Landau and E. M. Lifshitz, *Statistical Physics* (Pergamon, Oxford, 1959).
[43] M. E. Fisher, J. Phys. Soc. Jpn. **26**, 87 (1969).
[44] V. Privman and M. E. Fisher, J. Stat. Phys. **33**, 385 (1983).
[45] A. Vishnyakov and A. V. Neimark, J. Phys. Chem. B **105**, 7009 (2001).
[46] P. I. Ravikovitch, G. L. Haller, and A. V. Neimark, Adv. Colloid Interface Sci. **77**, 203 (1998).
[47] G. E. Norman and V. S. Filinov, High Temp. **7**, 216 (1969).
[48] B. K. Peterson and K. E. Gubbins, Mol. Phys. **62**, 215 (1987).
[49] J. W. Gibbs, *On the Equilibrium of Heterogeneous Substances Microform* (The Academy, New Haven, 1877).
[50] P. I. Ravikovitch, G. L. Haller, and A. V. Neimark, Stud. Surf. Sci. Catal. **117**, 77 (1998).
[51] A. V. Neimark, P. I. Ravikovitch, and A. Vishnyakov, Phys. Rev. E **65**, 031505 (2002).
[52] B. Widom, J. Chem. Phys. **39**, 2808 (1963).
[53] D. Reguera, R. K. Bowles, Y. Djikaev *et al.*, J. Chem. Phys. **118**, 340 (2003).
[54] G. M. Torrie and J. P. Valleau, J. Comput. Phys. **23**, 187 (1977).
[55] D. Frenkel and B. Smit, *Understanding Molecular Simulation: From Algorithms to Applications* (Academic, San Diego, 1996).